Transmission Electron Microscopy and Nanoindentation Study of the Weld Zone Microstructure of Diode-Laser-Joined Automotive Transformation-Induced Plasticity Steel

J. CHEN, K. SAND, M.S. XIA, C. OPHUS, R. MOHAMMADI, M.L. KUNTZ, Y. ZHOU, and D. MITLIN

We have used transmission electron microscopy (TEM) and nanoindentation to characterize the dominant phases present in the weld zone of a diode-laser-welded transformation-induced plasticity (TRIP) steel, examining the unaffected base metal as a baseline. The microstructure of the base metal consists predominantly of ferrite, retained austenite, martensite, and occasional large carbide particles. The dominant microstructure of the weld zone is of differently oriented packets having a bainitic morphology. The weld also contains allotriomorphic ferrite, idiomorphic ferrite, as well some twinned martensite that is surrounded by austenite. The TEM analysis of the bainitic-morphology packets indicates that they consist of a lath ferrite phase separated by an interlath carbon-enriched retained austenite. In most cases, the orientation relationship (OR) between the lath ferrite and the interlath retained austenite can be approximated as Nishiyama–Wasserman (N-W). We used site-specific nanoindentation to further characterize the packets and the allotriomorphic ferrite, confirming through the hardness values the conclusions reached by TEM. While martensite was regularly present in the base metal, it was only sparsely distributed within the weld zone, boding well for the weld's mechanical properties.

DOI: 10.1007/s11661-007-9389-x

I. INTRODUCTION

THE application of transformation-induced plasticity (TRIP) steels in automobile structures may be one of the critical breakthroughs allowing the simultaneous reduction in body weight and improvement in crash worthiness. The TRIP steels have multiphase microstructures consisting of ferrite, bainite, martensite, and carbon-enriched retained austenite.[1,2] The volume fraction of austenite varies with the composition and heat treatment, but it usually is on the order of 5 pct. As discussed in Reference 3, this hard-soft composite structure of TRIP steels leads to a combination of high strength and good uniform elongation. During forming, most of the retained austenite transforms to martensite, further boosting the material's work hardening. Steel automobile bodies and other structural components are assembled almost entirely by welding. Resistance spot welding (RSW) is a mature and established technology, currently one of the two dominant methods of auto body assembly. Laser welding is growing in importance as a potentially more productive alternative for automobile assembly due to the fast welding speed, excellent reproducibility of the joints, less distortion, reduced need for refinishing, and high joint rigidity. Similarly, to other fusion welding processes, laser welding generates a weld zone microstructure that significantly deviates from that of the base metal.

Studies of these laser-welded TRIP microstructures remain quite limited.[4–6] Han *et al.* studied 800 MPa class TRIP steel, welded by 4 kW-CO_2 laser beam, at welding speeds of 4 to 12 m/min.[4,5] They reported that when the welding speed was 4 m/min, the weld turned to full martensite. When welding speed further increased, resulting in a higher cooling rate, the strength and elongation remained constant. The authors in References 4 and 5 did not specify the cooling rate of the weld, making any processing-microstructure extrapolation quite difficult. Researchers have joined C-Mn steels by using high-power Nd:YAG laser beam at low welding speeds of 0.2 to 0.6 m/min.[6] The authors reported that the weld exhibited the microstructure of primarily acicular ferrite, plus allotriomorphic ferrite. Other phases, including bainite, were also reported present in the weld microstructure. Workers in References 4 through 6 characterized the microstructure using only light optical microscopy and scanning electron microscopy (SEM). Unfortunately, these techniques are not sufficiently accurate when applied to a TRIP steel microstructure due to its complexity and fine scale,

J. CHEN, Research Associate, K. SAND, Undergraduate Research Assistant, C. OPHUS and R. MOHAMMADI, Graduate Research Assistants, and D. MITLIN, Assistant Professor, are with the Department of Chemical and Materials Engineering, University of Alberta, and the National Institute for Nanotechnology, Edmonton, AB T6G 2G6, Canada. Contact e-mail: dmitlin@ualberta.ca M.S. XIA, Graduate Research Assistant, M.L. KUNTZ, Research Assistant Professor, and Y. ZHOU, Professor, are with the Department of Mechanical Engineering, University of Waterloo, Waterloo, ON N2L 3G1, Canada.

Manuscript submitted February 27, 2007.
Article published online February 5, 2008

providing insufficient quantitative information regarding the phases present, their orientation relative to each other, and their distribution within the weld. An accurate understanding of the processing-microstructure-properties relations in these fundamentally important materials requires detailed analysis by transmission electron microscopy (TEM), combined with site-specific nanomechanical testing of the individual phases.

In the current study, we initially diode laser beam weld an automotive-grade TRIP steel and then employ extensive TEM analysis, limited SEM characterization, and nanoindentation to detail the weld-zone microstructure. The welding parameters are meant to replicate the conditions potentially encountered in commercial automotive joining processes. In this work, we are specifically focusing on identifying the phases present within the weld zone, because this information is of utmost importance to welding engineers. The microstructure of the heat-affected-zone will be addressed in future correspondences. Here we also characterize the phases present in the unaffected metal, to be used as a baseline for our analysis.

II. EXPERIMENTAL

TRIP 780 steel was provided by the U.S. Steel Company (Pittsburgh, PA), and has the nominal composition Fe-0.15 wt pct C-2.09 wt pct Mn-1.73 wt pct Al-trace (Cr,Si,P). The sheets were 1.1-mm thick. Autogeneous butt welding was conducted with a diode laser power source. Butt welds were produced using a Nuvonyx ISL-4000 diode laser system (Bridgeton, MO) mounted on a Panasonic VR-16 welding robot (Matsushita Electric Industrial Co., Ltd., Osaka, Japan) at a welding speed of 1.6 m/min. The Nuvonyx ISL-4000 is a 4 kW AlGaAs diode laser with a wavelength of 805 ± 5 nm and a rectangular beam of 0.9 mm by 12 mm at the focal plane. The welding was carried out at the maximum power, *i.e.*, 4 kW. Argon was used as shielding gas from the top with the flow rate of 30 L/min. The weld was fully penetrated. The cooling rate in the fusion zone in the temperature range of 800 °C to 500 °C was estimated to be 53 °C/s, based on the thermal history of the weld that was modeled using a two-dimensional Rosenthal solution. This model is calibrated for coupling between the laser and work piece by comparing peak temperatures with the width of the heat-affected zone. A detailed description of the net power source estimation is reported elsewhere.[7]

The samples used for SEM examination were cut from the welded plate perpendicular to the welding direction, mounted, and then ground and polished using conventional metallographic methods. Final polishing was achieved with 0.05-μm alumina slurry. After that, samples were etched with 2 pct nital for about 20 seconds. A Hitachi S-3000 (Tokyo, Japan) was used for the SEM analysis. Thin-foil samples for TEM were prepared by mechanically thinning the welded steel to a thickness of approximately 50 μm and then punching into 3-mm discs. These discs were electropolished in a twin-jet electropolisher at room temperature (to retain any untransformed austenite). The TEM observations were performed on a JEOL* 2010 microscope operating at 200 kV. Selected-area electron diffraction (SAD) pattern simulation was done with the commercial software, Desktop Microscopist,** using the well-known crystallographic information of the different phases in steels.[8]

*JEOL is a trademark of Japan Electron Optics Ltd., Tokyo.

**Desktop Microscopist is a trademark of Desktop Microscopist.

The nanoindentation hardness measurements were performed using a Nano Indenter XP and MTS's (MTS Systems Corporation, Eden Prairie, MN) patented continuous stiffness measurement technique. A Berkovich indenter and constant strain rate were employed in the test. The nanopositioning stage and the Nano Indenter were employed to take the image (NANOVISION†) of the nanoindented sample. During the process, the tip of the indenter was held on the surface of the sample with a very small load. The nanopositioning stage was then translated in the x and y directions, while the indenter followed the topography of the sample surface in the z direction to create a three-dimensional image of the surface. The nanopositioning stage is a piezo-crystal driven x-y stage with closed-loop positioning control. The positioning feedback time is 2 ms. The travel range of the stage is 100 × 100 μm, and it is flat to within 2 nm across this range.

†NANOVISION is a trademark of MTS Systems Corporation, Eden Prairie, MN.

III. RESULTS

Figure 1 shows an SEM image of the as-received TRIP steel microstructure. From the morphology of the grains appearing in the SEM image, one cannot conclusively distinguish phases such as martensite or bainite. Hence, we did not label the separate phases in the image, rather relying on TEM for quantitative phase identification.

Figure 2 shows the TEM analysis of the as-received TRIP steel. Figure 2(a) shows a bright-field image of the microstructure. This image is representative of the microstructure generally encountered in the base metal of this TRIP steel. Figure 2(b) shows a symmetric SAD pattern obtained by tilting the labeled ferrite grain into its symmetric $[011]_\alpha$ zone axis. The axis was several degrees away from the orientation where the bright-field image in Figure 2(a) was obtained. Figure 2(c) shows a dark-field image of grain boundary retained austenite (labeled γ) adjacent to a packet of martensite. The image was obtained using a strong $g = \bar{2}00_\gamma$ reflection, near the

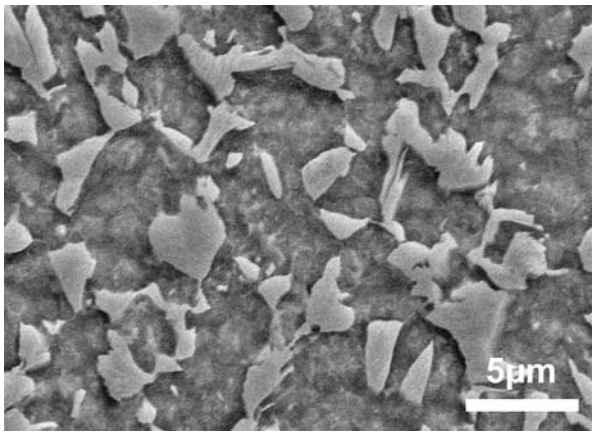

Fig. 1—Scanning electron micrograph of the as-received TRIP steel.

$[001]_\gamma$ zone axis. Because the misalignment of twinned lamellas of martensite (visible in the lower right corner and marked by an arrow) causes arc type spots in the SAD pattern, the martensite also showed strong dark-field contrast. Figure 2(d) shows the SAD pattern and its simulation for the austenitic grain shown in Figure 2(c). The sample is oriented near the $[001]_\gamma$ zone axis, but with the $g = \bar{2}00_\gamma$ row strongly excited. An arrow points to the particular $\bar{2}00_\gamma$ reflection used to create the image. In the SAD, the first $g = \bar{2}00_{\alpha'}$ reflection is rotated approximately 8 deg clockwise relative to $g = \bar{2}20_\gamma$, while the second is rotated 8 deg counterclockwise. The SAD in Figure 2, and in the subsequent figures, was not oriented to account for rotation calibration.

Figure 3 demonstrates the typical distribution of ferrite observed in the base metal. The dark-field image in Figure 3(a) highlights several ferrite laths that have a similar orientation within the matrix. Figure 4 shows a bright-field and a dark-field image of a representative packet of twinned martensite. The corresponding SAD pattern and its simulation are presented in Figure 4(c). The dark-field image of the twinned martensite was obtained by using the reflection streak marked by an arrow in the SAD pattern. Twinned martensite, while being a minority phase, was commonly observed in the base metal. The formation of twinned martensite is generally related to the carbon concentration of the steel.[9] The twinned structure of martensite in such low-carbon TRIP steel is due to the carbon partitioning between the ferrite and the austenite in the isothermal bainitic transformation stage in TRIP steel manufacturing. This leads to the formation of twinned martensite when the carbon concentration in the austenite exceeds a certain critical value.

Figures 5(a) and (b) show the bright-field and dark-field images of several carbides present within a grain boundary (arrowed in 5(a)). Such carbides were periodically observed in the base metal. At least three carbides are visible just in this bright-field image. Using the same dark-field reflection, $g = \bar{1}21_{M_3C}$, we were able to image two carbides simultaneously. The carbide that was analyzed analytically is marked by the asterisked-arrow in Figure 5(a). Figure 5(c) shows the experimental and simulated diffraction pattern of this carbide in its [12-3] zone axis. The energy dispersive spectrum of M_3C (M = Fe, Mn) is shown in Figure 5(d), which indicates that the carbide is Fe-rich, while containing secondary amounts of Mn. Trace Cr was also detected from this region.

Figure 6 shows an SEM micrograph of a representative microstructure of the weld zone. Allotriomorphic ferrite and idiomorphic ferrite can be identified based on their characteristic morphology. Packets containing aligned lath structure are also visible in this micrograph. These aligned lath structures are similar in morphology to what was previously reported to be bainite in TRIP steels,[1,10,11] and can be referred to as "bainitic" based on their morphology, without actually specifying the constituent phases. The label does not necessarily mean the strict "classic" definition of bainite,[12] as composed of ferrite and Fe_3C, but rather indicates a certain morphology of the phases. In fact, we will show in our subsequent TEM and nanoindentation analysis that there is no ferrite-Fe_3C bainite within the weld.

Figure 7(a) shows the bright-field TEM image of the bainitic structure, which is actually composed of ferrite laths and of interlath austenite. Figure 7(b) shows a dark-field image of the interlath austenite phase, taken using the $g = \bar{1}1\bar{1}_\gamma$ reflection. The symmetric SAD pattern shown in Figure 7(c) was obtained by tilting several degrees away from the orientation where the dark-field image was obtained. Figure 7(c) indicates that the parent interlath retained austenite phase has a Nishiyama–Wasserman (N-W) orientation relationship (OR) with the aligned ferrite lath. The N-W OR is one of the most frequently reported relationships for the fcc-bcc systems. In this orientation, the closest-packed planes of the fcc and bcc phases are parallel ($\{111\}_{fcc}//\{110\}_{bcc}$), and the close-packed direction of the fcc phase is aligned with the cube edge of the bcc phase ($\langle 110\rangle_{fcc}//\langle 100\rangle_{bcc}$). There are 12 variants of the N-W OR. We should indicate, however, that both the N-W and the Kurdjumov–Sachs (K-S) ORs are fundamentally approximations. It is known that the true orientation relation between ferrite and austenite is irrational, with the closest packed planes being not quite parallel in order to give an invariant line between the two phases.[13]

Figure 8(a) shows a bright-field image of the structure in another bainitic packet. When using $g = 0\bar{1}1_\alpha$ reflection, we obtained a dark-field image of an aligned ferrite lath (Figure 8(b)). We obtained the dark-field image of the retained austenite phase by using $g = \bar{1}1\bar{1}_\gamma$ refection (Figure 8(c)). In all our observations of the bainitic packets, the retained austenite was always present as a film between the laths. The experimental SAD pattern and simulation in Figure 8(d) indicates that the orientation relation between the two phases is again approximated as N-W. However, we did infrequently detect other orientation relations between the austenite film and the ferrite laths, including the K-S and $(1\bar{1}\bar{1})_\gamma//(01\bar{1})_{\alpha_2}$, $[211]_\gamma//[311]_{\alpha_2}$.

Figure 9 shows a bright-field image of twinned martensite in the weld zone. The SAD pattern and its simulation are also shown beside the image. Two twin variants of martensite are visible in the SAD, having the

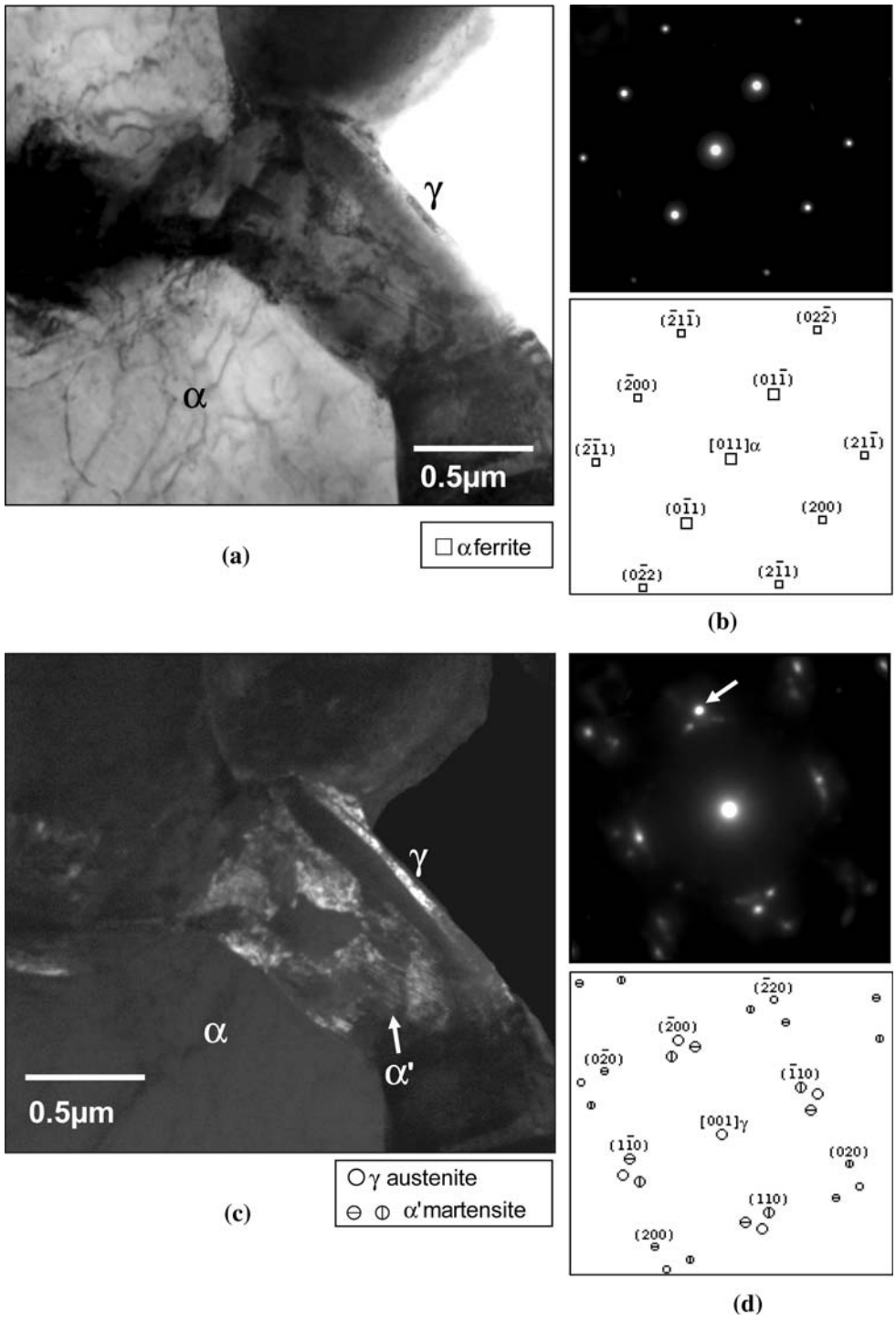

Fig. 2—Base metal. (*a*) Bright-field image of several ferritic grains along with retained austenite at the grain boundary. (*b*) SAD pattern and its simulation of a ferritic grain labeled α in (a). To capture the symmetric zone axis SAD, the sample was tilted several degrees away from its orientation in the bright-field image (a). (*c*) Dark-field image of the retained austenite phase labeled γ in (a). The image was obtained by using the $g = \bar{2}00_{\gamma}$ reflection near the $[001]_{\gamma}$ zone axis. Also visible in the dark-field image is a packet of twinned martensite, labeled α′. (*d*) SAD and its simulation of the austenitic grain labeled γ in (c). The sample is oriented near the $[001]_{\gamma}$ zone axis, with the $g = \bar{2}00_{\gamma}$ row strongly excited. Also visible in the SAD are the twinned martensite reflections, which were captured by the objective aperture during imaging.

following OR with each other: $(\bar{1}21)_{\alpha'}//(2\bar{1}1)_{\alpha'T}$, $[311]_{\alpha'}//[\bar{1}13]_{\alpha'T.}$ Unlike the case of the base metal, martensite is not frequently observed within the weld zone. Figure 10 displays low-magnification images of the weld zone region containing martensite (marked by an arrow in the images) surrounded by austenite. Such regions constituted a much smaller fraction of the overall microstructure than did the bainitic packets.

Figure 11 presents the NANOVISION image of the region where the six site-specific nanoindents were

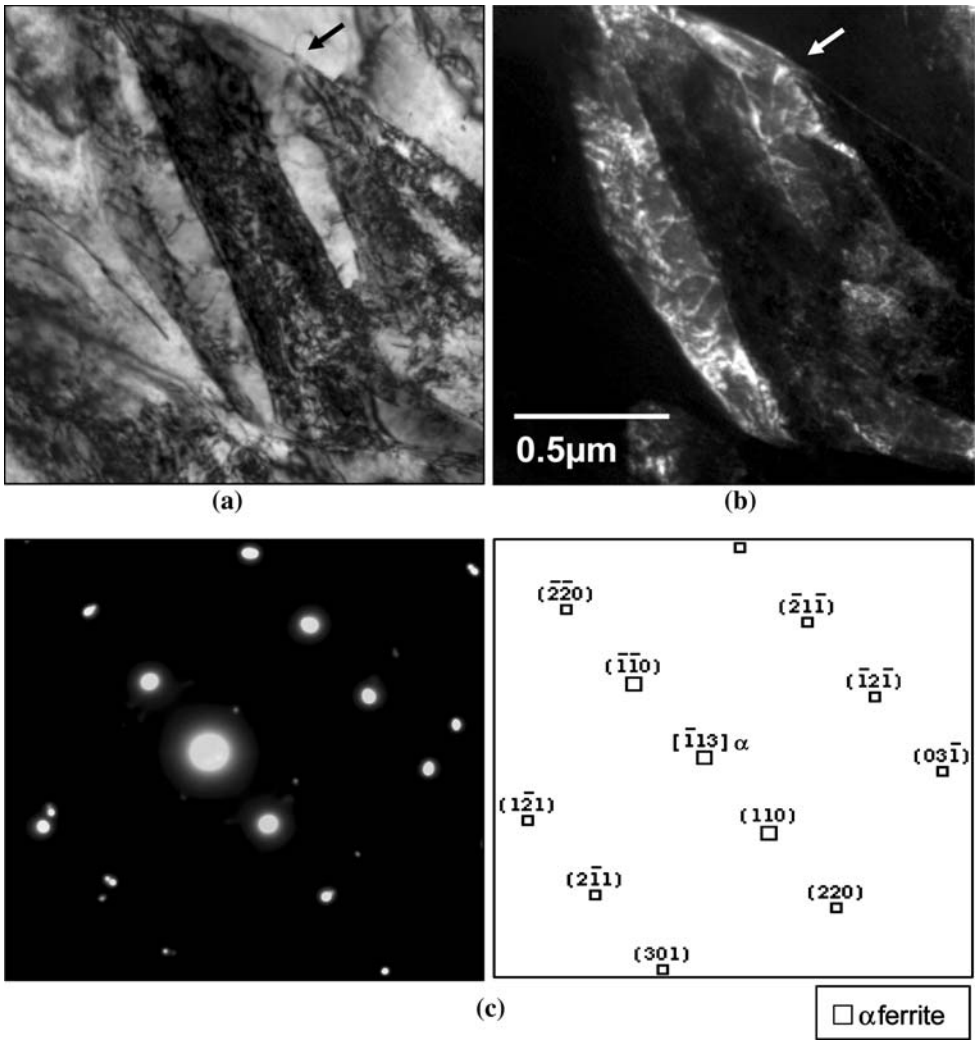

Fig. 3—Base metal. (*a*) and (*b*) Bright-field and dark-field images of the ferrite microstructure found in the base metal. The dark-field image was taken near the $[\bar{1}13]_\alpha$ zone axis, using the $g = 03\bar{1}_\alpha$ reflection. Arrows point to the same location in the two micrographs. (*c*) Symmetric zone axis SAD of the ferrite grains and the corresponding simulation.

performed (arrowed). Three indents were conducted in the dark region in the center of the image, which, judging by its morphology, is allotriomorphic ferrite. The other three indents were performed in the bainitic packets. Figure 12(a) shows the load-displacement curves for the six indents, while Figure 12(b) presents the derived nanoindentation hardness values. The six corresponding load-displacement curves can be separated into two groups. The first group includes curves 1, 3, and 5, and corresponds to the indents performed on the ferrite; the second group includes curves 2, 4, and 6 and corresponds to the indents performed on the bainite. The nanoindentation hardness of the first group ranges from 2.6 to 3.1 GPa, with a mean of 2.98 ± 0.29 GPa. The nanoindentation hardness of the second group ranges from 4.3 to 5.5 GPa, with a mean of 4.95 ± 0.61 GPa.

There are two previous reports on nanoindentation of TRIP steels.[14,15] Researchers in Reference 14 reported martensite to the have the highest nanoindentation hardness of 16.7 ± 1.9 GPa, followed by retained austenite (10.0 ± 1.1 GPa), bainite (7.0 ± 0.8 GPa), and ferrite (4.8 ± 0.2 GPa). Other workers[15] obtained a nanoindentation hardness of 3.7 GPa for ferrite and 7.5 GPa for bainite.[16] The absolute hardness values are difficult to compare between each study, because a different steel alloy was used in each case (this work, Fe-0.15C-2.09Mn-1.73Al; Reference 14, Fe-0.29C-1.42Mn-1.41Si; Reference 15, Fe-0.20C-1.50Mn-1.50Si). In addition, References 14 and 15 used different nanoindentation tip geometries than we did, and tested using smaller final loads (current study 5 to 6 mN *vs* 250 to 500 μN). However, what we can safely conclude is that the difference between the hardness of martensite and ferrite is much more significant than the difference between the hardness of bainite and ferrite. Thus, the nanoindentation results substantiate the TEM analysis of the bainitic packets.

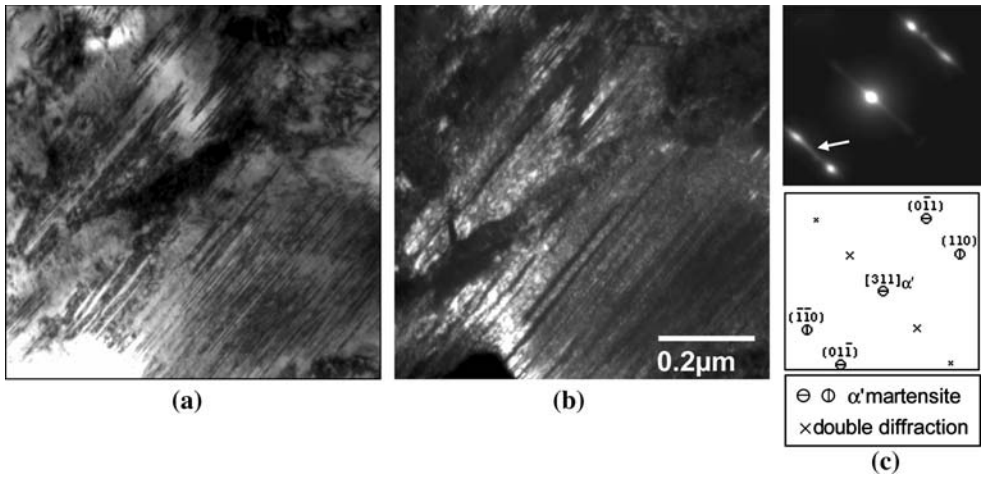

Fig. 4—Base metal: (*a*) and (*b*) show bright field and dark field micrographs of twinned martensite. The dark-field image was obtained by using the streak marked by the white arrow on the SAD pattern (*c*). The SAD is actually a composite diffraction pattern, showing two orientation variants of martensite: $[311]_{\alpha'1}//[\bar{1}13]_{\alpha'2}$ $(\bar{1}21)_{\alpha'1}//(2\bar{1}1)_{\alpha'2}$.

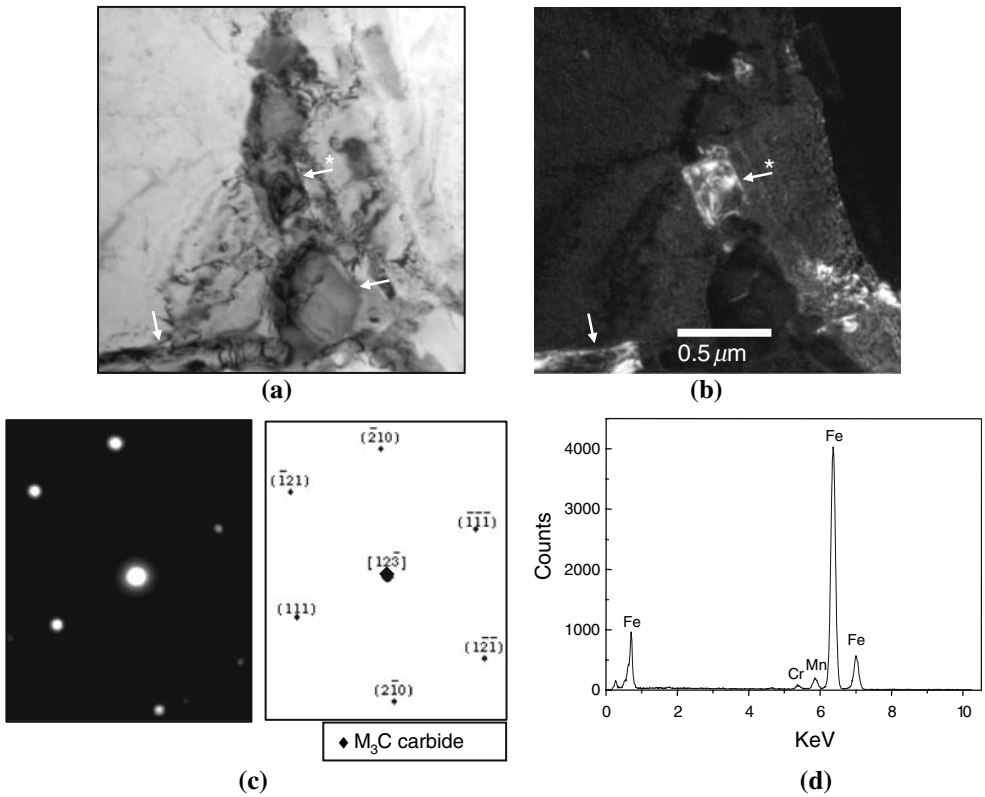

Fig. 5—Base metal. (*a*) and (*b*) Bright-field and dark-field ($g = \bar{1}21_{M_3C}$) images of several M_3C carbides. (*c*) Corresponding SAD pattern and simulation. (*d*) Energy dispersive spectrum obtained from the middle carbide (asterisked arrow).

IV. DISCUSSION

Figures 7 and 8 demonstrate that the bainite packets found in the weld consist of aligned ferrite laths separated by films of retained austenite. Only a minor amount of martensite is present within the weld and no carbides were detected. The weld microstructure depends both on the steel's composition and on the cooling rate of the weld. We will first discuss the composition effect. According to References 12 and 20, bainite consists of ferrite platelets in sheaves, separated by cementite. However, with the appropriate alloying additions, cementite may be replaced by retained austenite or martensite.[12,20] In TRIP 780, the key alloying additions for stabilizing austenite and preventing the

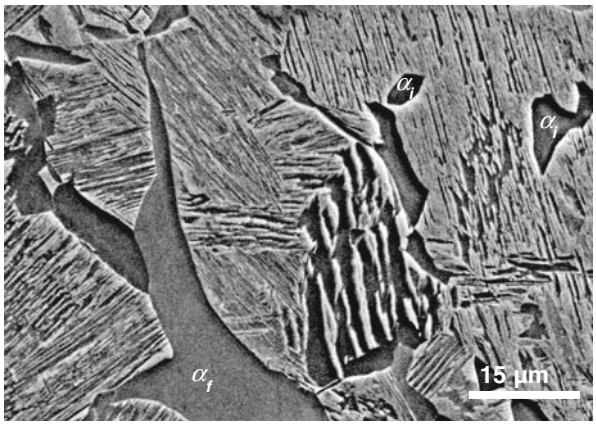

Fig. 6—SEM micrograph of the weld zone, displaying variously aligned "bainitic" packets, allotriomorphic ferrite grains (α_f), and idiomorphic ferrite grains (α_i).

formation of carbides are aluminum and manganese.[16–19] Silicon would also have a significant effect if it were present in larger quantities.[18] Aluminum is known to decrease the activity and increase the solubility of carbon in ferrite, reducing the driving force for carbide precipitation.[18] Manganese will also stabilize austenite by reducing the activity of carbon in ferrite and austenite and increasing the carbon solubility in ferrite.[18,19] Both elements therefore will lower the cementite precipitation starting temperature. The difficulty in forming martensite comes from the synergy of carbon and aluminum.[18] Carbon is known to play a key role in austenite stabilization by decreasing the starting temperature of martensite transformation M_s.[12,16] During the process of bainitic reaction, when upper bainite is formed, carbon is rejected by the ferrite and is partitioned into the untransformed austenite. While the carbon content of this steel is relatively low,

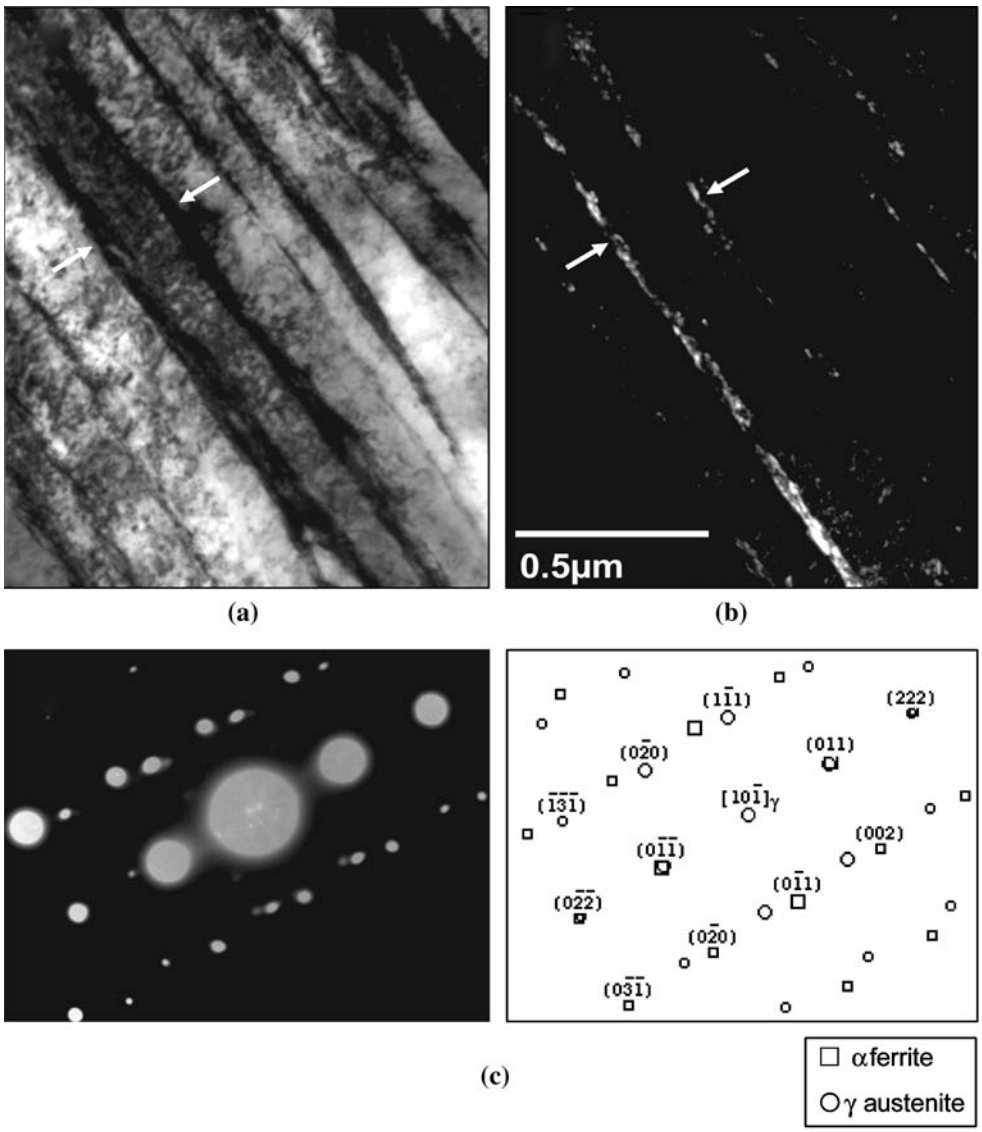

Fig. 7—Weld zone. (*a*) and (*b*) Bright-field and dark-field ($g = \bar{1}1\bar{1}_\gamma$) images of a bainitic packet, which is a composite of heavily dislocated ferrite laths and interlath austenite. Arrows point to the same region in the two micrographs. (*c*) Symmetric SAD and the corresponding simulation of the orientation relation between the austenite and the ferrite, which can be approximated as N-W.

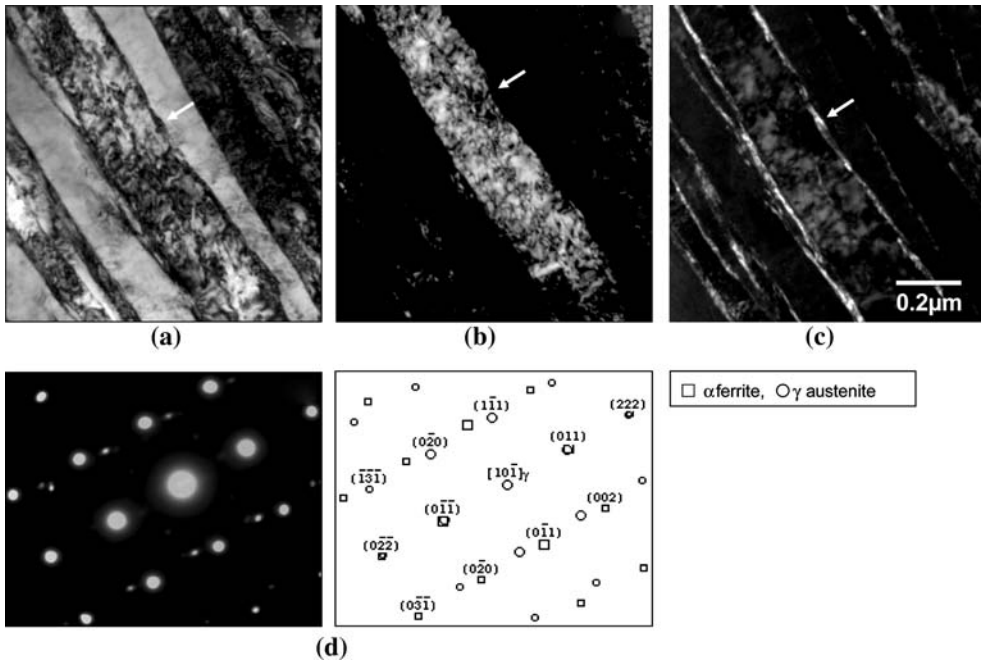

Fig. 8—Weld zone. (*a*) Bright-field image of the bainitic structure. (*b*) Dark-field image of a ferritic lath ($g = 0\bar{1}1_{\alpha}$). (*c*) Dark-field image of the interlath retained austenite ($g = \bar{1}1\bar{1}_{\gamma}$). The symmetric SAD and simulation again demonstrates the N-W orientation relationship between the retained austenite and the ferrite. Arrows point to the same location in the micrographs.

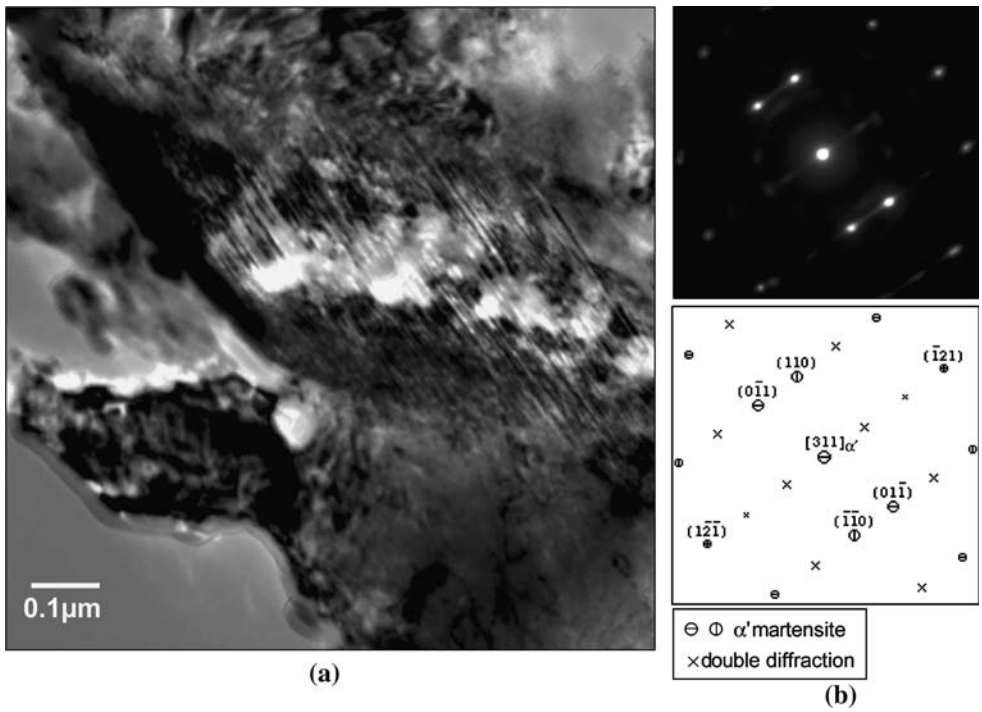

Fig. 9—Weld zone. (*a*) Bright-field micrograph of twinned martensite. (*b*) Corresponding composite SAD pattern and simulation: $[3\bar{1}1]_{\alpha'1}//[\bar{1}13]_{\alpha'2}$ $(\bar{1}21)_{\alpha'1}//(2\bar{1}\bar{1})_{\alpha'2}$.

its diffusion into the austenite films will help to stabilize them. The presence of aluminum will have a synergistic effect, resulting in enhanced carbon content within the retained austenite.[18]

Existing studies on the microstructures of welded TRIP steels remain quite limited, relying solely on SEM or light-optical analysis for their conclusions. For example, recent analysis based on SEM observations

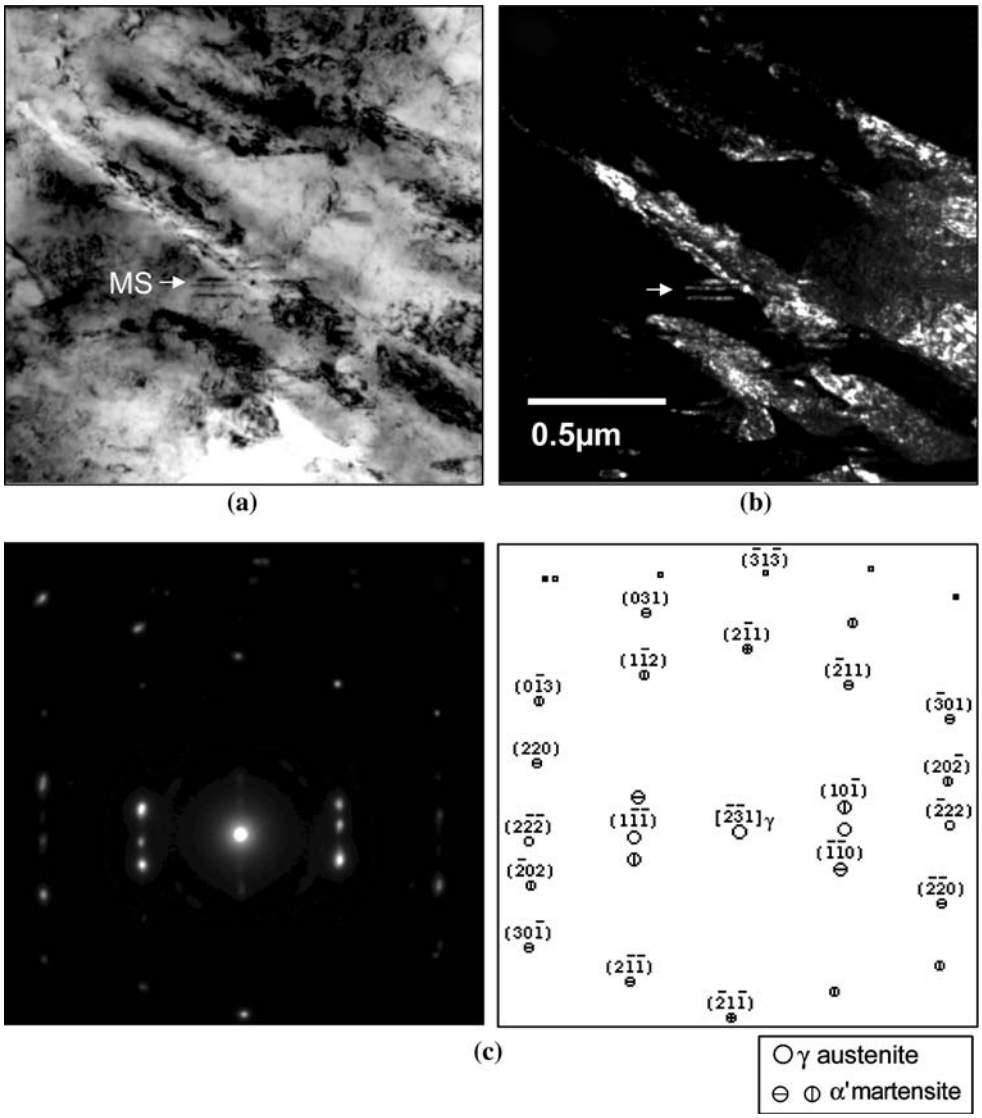

Fig. 10—Low-magnification image of the weld zone, in a martensite plus austenite region. (*a*) Bright-field image of twinned martensite (arrowed) in an austenitic matrix. (*b*) Dark-field image of twinned martensite ($g = \bar{1}\bar{1}0_{\alpha'}$). Some intensity from the austenite reflection $g = \bar{1}11_{\gamma}$ is also captured in the aperture. (*c*) The SAD pattern and its simulation.

indicated that the 4 kW-CO_2 laser-beam-welded structure of a TRIP 800 steel was fully martensitic.[4] However, it is highly doubtful that SEM analysis can properly distinguish between martensite and heavily dislocated ferrite. It is therefore not possible to provide direct and meaningful comparisons of our findings with literature.

There have been reports on the formation of lath martensite-interlath retained austenite film structure in silicon or manganese containing steels.[21,22] However, although high dislocation density can be revealed within the laths (Figure 8, for example), this does not mean the laths are martensitic, because high dislocation density can exist in bainitic ferrite as well.[12,19,20] Historically, researchers have had difficulties in conclusively identifying dislocated ferrite from dislocated martensite. This is largely due the inability of selected area diffraction in a TEM to resolve the small differences between the lattice parameters of the two. One way researchers have in the past attempted to distinguish between the two phases is through their ''characteristic'' morphology. Some researchers proposed several criteria according to the morphology difference.[23,24] These relied largely on the lath ferrite morphology, which is usually coarse, curved, or wavy, as well as considerations of the number of lath variants within each packet. However, recent studies have concluded that martensite could also have a coarse morphology[25] and similar number of variants as the ferrite.[26] It is thus quite advantageous to combine TEM and site-specific nanoindentation to not only probe the morphology and crystallography of the fine structure, but to provide complementary site-specific nanomechanical data to identify the phases.

The second factor that determines the degree of martensite presence within the weld is the cooling rate. The cooling rate of the weld depends on the heat

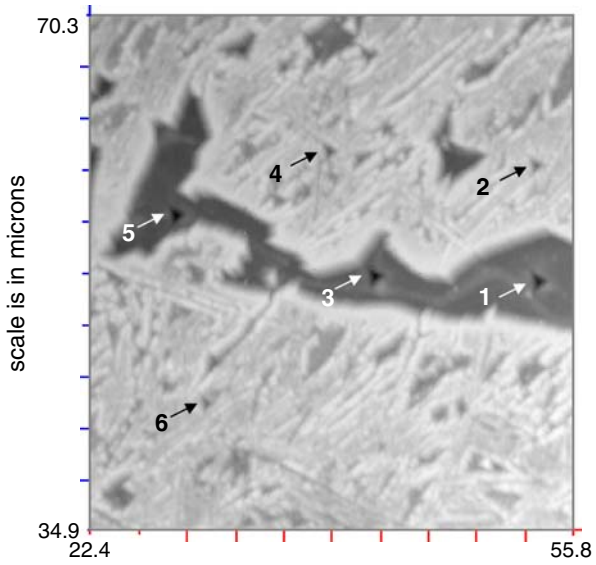

Fig. 11—NANOVISION image of the nanoindented area; the indents are marked 1–6.

(power) input, welding speed, and the geometry of the steel to be welded. Most recently, authors have calculated the critical cooling rates of martensite formation for several advance high-strength steels (AHSS) subjected to different welding processes, such as RSW, resistance mash seam welding (RMSEW), and laser beam welding (LBW).[27] The calculated critical cooling rate for martensite formation varies from 70 °C/s to 13,500 °C/s, depending on the compositions of the steels. Among them, the predicated martensite formation critical cooling rate for TRIP 800 steel is 90 °C/s. Because the TRIP steel in this study has similar in composition to TRIP 800, 90 °C/s may be used as the reference critical cooling rate for the formation of a fully martensitic weld. This rate is greater than the estimated 53 °C/s cooling rate in the current welding process.[28] Therefore, the dominant phase in the weld should not be martensite, agreeing with our experimental results.

Twinned martensite is well known to lead to brittle fracture due to the blockage of slip bands by twin boundaries, stress concentration, and microcrack formation, where twinning is arrested or elastic-plastic disturbances as a result of twin propagation (*e.g.*, Reference 29). Thus, from a properties viewpoint, it is quite beneficial that fairly little twinned martensite is present within this weld.

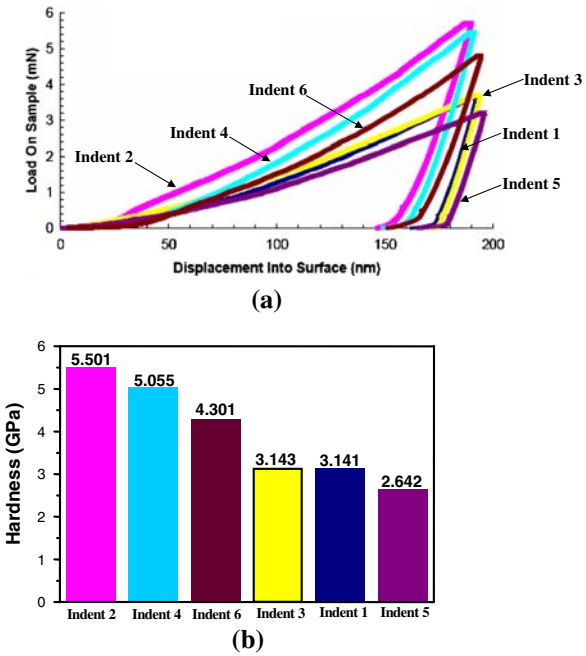

Fig. 12—(*a*) Load-depth curves for the six nanoindentations. (*b*) Derived hardness results.

V. CONCLUSIONS

We used TEM analysis, SEM analysis, and site-specific nanoindentation to detail the microstructure of a diode-laser-welded automotive TRIP steel. We found that in the base metal, the microstructure consists of a mixture of ferrite grains, martensite, retained austenite, and occasional carbides.

The weld zone largely consists of variously oriented bainitic-morphology packets. The weld zone also contains allotriomorphic ferrite, idiomorphic ferrite, and martensite that are surrounded by austenite. Detailed TEM analysis revealed that the bainitic packets are composed of a lath ferrite phase and an interlath retained austenite phase. The retained austenite and the ferrite have an OR that could be approximated by the well-known N-W OR, though other ORs were also detected.

We used nanoindentation to site specifically mechanically test the bainitic packets and the allotriomorphic ferrite, confirming by the hardness values that the packets are indeed composed of ferrite rather than martensite laths. The martensite that is present in the weld has a similar morphology to the martensite in the base metal but is present in a much lower volume fraction.

ACKNOWLEDGMENTS

We are very grateful to Harry Bhadeshia and Velimir Radmilovic for the critical presubmission reviews of this manuscript. We also thank Ryan O'Hagan, MTS, for assistance with the nanoindentation testing and for very useful discussions. One of the authors (JC) wants to thank Dr. Fu-Gao Wei, National Institute for Materials Science of Japan, for the discussion. This research is financially supported by the Natural Sciences and Engineering Research Council (NSERC) of Canada and AUTO21 Network Centres of Excellence of Canada.

REFERENCES

1. S. Zaefferer, J. Ohlert, and W. Bleck: *Acta Mater.*, 2004, vol. 52, pp. 2765–78.
2. P.J. Jacques: *Curr. Opin. Solid State Mater. Sci.*, 2004, vol. 8, pp. 259–65.
3. H.K.D.H. Bhadeshia: *ISIJ Int.*, 2002, vol. 42, pp. 1059–60.
4. T.K. Han, S.S. Park, K.H. Kim, C.Y. Kang, I.S. Woo, and J.B. Lee: *ISIJ Int.*, 2005, vol. 45, pp. 60–65.
5. T.K. Han, K.H. Kim, B.I. Kim, C.Y. Kang, I.S. Woo, and J.B. Lee: *Mater. Sci. Forum*, 2004, vols. 449–452, pp. 409–12.
6. P.L. Moore, D.S. Howse, and E.R. Wallach: *6th Int. Conf. on Trends in Welding Research*, Pine Mountain, GA, May 2002, oral presentation and private communication.
7. S. Lawson, X. Li, and Y. Zhou: *Sheet Metal Welding Conf. XII*, Livonia, MI, May 2006, p. 9.
8. K.W. Andrews, D.J. Dyson, and S.R. Keown: *Interpretation of Electron Diffraction Patterns*, 2nd ed., Plenum Press, New York, NY, 1971, pp. 210–11.
9. G.R. Speich and W.C. Leslie: *Metall. Trans.*, 1972, vol. 3, p. 1043.
10. A.Z. Hanzaki, P.D. Hodgson, and S. Yue: *Metall. Mater. Trans. A*, 1997, vol. 28A, pp. 2405–14.
11. B. Verlinden, P. Bocher, E. Girault, and E. Aernoudt: *Scripta Mater.*, 2001, vol. 45, pp. 909–16.
12. R.W.K. Honeycombe and H.K.D.H. Bhadeshia: *Steels Microstructure and Properties*, 2nd ed., Butterworth Heinemann, Oxford, United Kingdom, 2000, pp. 115–39.
13. H.K.D.H. Bhadeshia: private communication, University of Cambridge, UK, Dec 2006.
14. Q. Furnemont, M. Kempf, P.J. Jacques, M. Goken, and F. Delannay: *Mater. Sci. Eng. A*, 2002, vol. 328, pp. 26–32.
15. J. Angeli and A.C. Kneissl: *Z. Metallkd.*, 2004, vol. 95, pp. 601–06.
16. M. De Meyer, D. Vanderschueren, and B.C. De Cooman: *ISIJ Int.*, 1999, vol. 39, pp. 813–22.
17. H.K.D.H. Bhadeshia and D.V. Edmonds: *Metall. Trans. A*, 1979, vol. 10A, pp. 895–07.
18. B.C. De Cooman: *Curr. Opin. Solid State Mater. Sci.*, 2004, vol. 8, pp. 285–03.
19. R.W.K. Honeycombe and F.B. Pickering: *Metall. Trans.*, 1972, vol. 3, p. 1099.
20. H.K.D.H. Bhadeshia: *Bainite in Steels: Transformations, Microstructure and Properties*, 2nd ed., IOM Communications, Ltd., London, 2001, pp. 19–61.
21. T. Maki and C.M. Wayman: *Acta Metall.*, 1977, vol. 25, pp. 695–710.
22. T.V. Eterashvili, L.M. Utevskiy, and M.N. Spasskiy: *Fiz. Met. Metall.*, 1979, vol. 48, pp. 807–15.
23. G. Spanos, R.W. Fonda, R.A. Vandermeer, and A. Matuszeski: *Metall. Mater. Trans. A*, 1995, vol. 26A, pp. 3277–93.
24. R.W. Fonda and G. Spanos: *Metall. Mater. Trans. A*, 2000, vol. 31A, pp. 2145–53.
25. P.M. Kelly, A. Jostsons, and R.G. Blake: *Acta. Metall. Mater.*, 1990, vol. 38, pp. 1075–81.
26. S. Morito, H. Tanaka, R. Konishi, T. Furuhara, and T. Maki: *Acta Mater.*, 2003, vol. 51, pp. 1789–99.
27. J.E. Gould, S.P. Khurana, and T. Li: *Welding J.*, 2006, vol. 85, pp. 111S–116S.
28. O. Akselsen, O. Grong, and J. Solberg: *Mater. Sci. Technol.*, 1987, vol. 3, pp. 649–55.